*International Journal of Minerals, Metallurgy and Materials*
*Volume 27, Number 2, February 2020, Page 252*
**https://doi.org/10.1007/s12613-019-1902-x**

# Mechanical characterization of Mg−$B_4C$ nanocomposite fabricated at different strain rates

*Gholam Hossein Majzoobi and Kaveh Rahmani*

Mechanical Engineering Department, Bu-Ali Sina University, Hamedan 65174, Iran
(Received: 5 July 2019; revised: 21 September 2019; accepted: 24 September 2019)

**Abstract:** Magnesium has wide application in industry. The main purpose of this investigation was to improve the properties of magnesium by reinforcing it using $B_4C$ nanoparticles. The reinforced nanocomposites were fabricated using a powder compaction technique for 0, 1.5vol%, 3vol%, 5vol%, and 10vol% of $B_4C$. Powder compaction was conducted using a split Hopkinson bar (SHB), drop hammer (DH), and Instron to reach different compaction loading rates. The compressive stress–strain curves of the samples were captured from quasi-static and dynamic tests carried out using an Instron and split Hopkinson pressure bar, respectively. Results revealed that, to achieve the highest improvement in ultimate strength, the contents of $B_4C$ were 1.5vol%, 3vol%, and 3vol% for Instron, DH, and SHB, respectively. These results also indicated that the effect of compaction type on the quasi-static strength of the samples was not as significant, although its effect on the dynamic strength of the samples was remarkable. The improvement in ultimate strength obtained from the quasi-static stress–strain curves of the samples (compared to pure Mg) varied from 9.9% for DH to 24% for SHB. The dynamic strength of the samples was improved (with respect to pure Mg) by 73%, 116%, and 141% for the specimens compacted by Instron, DH, and SHB, respectively. The improvement in strength was believed to be due to strengthening mechanisms, friction, adiabatic heating, and shock waves.

**Keywords:** powder compaction; $B_4C$; magnesium; strain rate; ultimate strength; sintering

## 1. Introduction

Magnesium and its alloys are attractive in automobile and aerospace industries due to their light weight and low fuel consumption. However, its low corrosion resistance and relatively poor mechanical properties have restricted its application in industry [1]. Therefore, attempts have been made to improve the properties of magnesium by reinforcing it with nanoparticles, such as SiC and $B_4C$. The literature indicates that mechanical properties of magnesium-based nanocomposites reinforced by ceramic nanoparticles can be improved without losing their malleability [2]. The main challenge in adding nanoparticles is clustering that occurs, leading to nonuniform distribution and agglomeration of particles in the metal matrix. This phenomenon can be controlled by a proper sintering procedure and using ultrasonic vibrations [3]. Various methods, including ultrasonic cavitation-assisted solidification [4], *in-situ* sintering [5], *in-situ* intercalation [6], *in-situ* polymerization [7–8], etc., can be used to fabricate nanocomposites. Also, there are several methods for fabrication of magnesium alloys reinforced by nanoparticles, the most common being powder metallurgy [9], hot extrusion [10], cold press, and normal sintering [11]. However, the powder metallurgy technique is believed to be simpler than the other approaches, thereby resulting in its widespread use in industry [9]. This technique may be used under quasi-static conditions, which often requires hot sintering after or during the fabrication process. Composite materials can also be manufactured through high velocity compaction (HVC) techniques using dynamic methods or shock-wave consolidation. The main advantage of these methods is that they often (though not always) eliminate hot sintering from the production cycle. HVC methods often use explosion or gas pressure in order to accelerate a projectile or the impact of a drop hammer (DH) in order to compact powders. The mass of dropping hammer varies from 5 to around 1200

Corresponding author: Gholam Hossein Majzoobi E-mail: gh_majzoobi@yahoo.co.uk, gh_majzoobi@basu.ac.ir

kg, and the impact velocity also varies between 2 and 30 m/s [12]. Unlike the common quasi-static methods, dynamic processes make it possible to create the high local and instantaneous temperatures needed for formation of metallurgical bonds between particles while keeping other areas at a low temperature. Therefore, dynamic compaction techniques can minimize microstructural changes, including clustering and grain growth, which may occur at elevated temperatures [13]. Farughi *et al.* [14] used underwater shockwaves to produce a Mg–SiC composite. Majzoobi *et al.* [15–16] and Rahmani *et al.* [17] also used dynamic equipment for compacting nanocomposites. Several studies have been reported on the effects of $B_4C$ particles on the mechanical properties of Mg in the literature. Jiang *et al.* [18] investigated the fabrication of $B_4C$ particulate-reinforced Mg using powder metallurgy (P/M). They reported improvement in the hardness of Mg reinforced by 10vol% to 15vol% $B_4C$. Aydin *et al.* [19] studied the effect of nano- and micro-sized $B_4C$ reinforcement on the mechanical properties of Mg–$B_4C$ nanocomposite using powder metallurgy. They showed that the reinforcements could improve the mechanical properties of Mg–$B_4C$ composites. Aatthisugan *et al.* [20] produced AZ91D–$B_4C$ composites using the stir casting method. They reported improvement in the hardness of AZ91D–$B_4C$ samples. Kevorkijan and Škapin [21] studied the tensile and hardness behavior of compacted Mg–$B_4C$ composite and showed that reinforcement could improve the tensile and hardness of the composites. Yao *et al.* [22] also investigated the hardness behavior of $B_4C$-reinforced Mg-matrix composites fabricated by the metal-assisted pressureless infiltration technique.

In this study, Mg–$B_4C$ nanocomposites were fabricated using three methods including: (1) hot dynamic compaction using split Hopkinson bar, (2) hot dynamic compaction using a DH, and (3) hot quasi-static compaction using Instron. Furthermore, the effects of the content of reinforcing nanoparticles on the strength of Mg–$B_4C$ nanocomposites under different loading rates (quasi-static and dynamic) were investigated.

## 2. Experimental

### 2.1. Materials

The aim of this study was to strengthen magnesium powder using boron carbide nanoparticles ($B_4C$ nanoparticles with an average size of 45 nm and spherical morphology) with a purity of 99.99%. Previous investigations have indicated that the particles with an average size <100 μm and an irregular morphology may yield higher density [11]. Therefore, the magnesium powder with a particle size between 75 and 150 μm, purity of 99.5%, and irregular morphology was purchased from Merck Co., Ltd., Germany. Fig. 1 shows the scanning electron microscopy (SEM) images of the magnesium powder at two different magnifications. As can be seen, the particles had an irregular morphology with a particle size of approximately 100 μm. Fig. 2 shows the SEM image of the nanosize $B_4C$ nanoparticles.

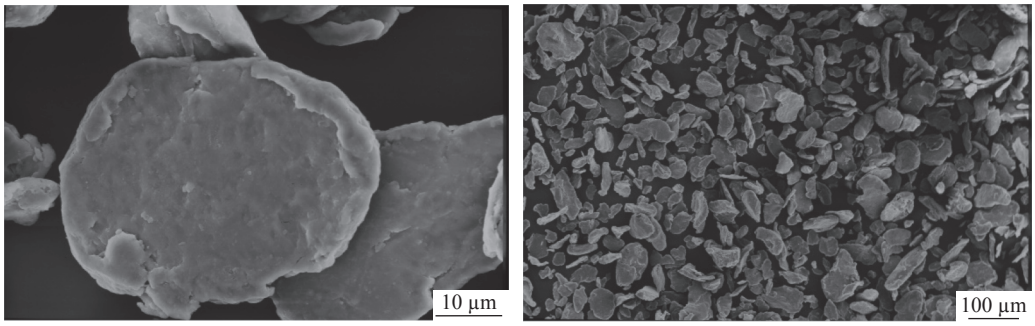


**Fig. 1. SEM micrographs of Mg particles at two magnifications.**

In order to prevent clustering of nanoparticles and reach a uniform particle distribution, an ultrasonic process was employed to disperse the $B_4C$ nanoparticles in the matrix. To do this, after manually mixing the desired amounts of nanoparticles (0, 1.5vol%, 3vol%, 5vol%, and 10vol%) with the magnesium powder in a glovebox, ethanol was added to the mixture. The mixture was then placed in an ultrasonic bath for 20 min. In the next step, the mixture was dried in an oven at 323 K. 35 g of the mixed powder was then combined with 0.5wt% stearic acid in a planetary ball mill with a 125 mL compartment for 1 h under an argon atmosphere. Table 1 shows the milling conditions and properties of the powders used in the experiments.

### 2.2. Fabrication method for Mg–$B_4C$ nanocomposites

In order to produce the nanocomposite samples, hot quasi-static compactions were conducted using an Instron testing machine at a strain rate ($\dot{\varepsilon}$) of $8 \times 10^{-3}$ $s^{-1}$. Hot dy-

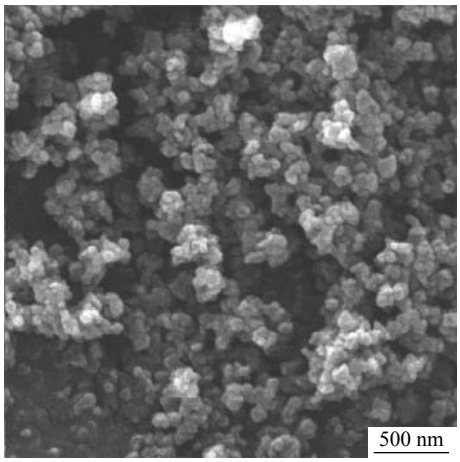


**Fig. 2. SEM micrograph of $B_4C$ nanoparticles.**

namic compactions were carried out using a drop hammer and a split Hopkinson bar at strain rates of $8 \times 10^2$ and $1.6 \times 10^3$ $s^{-1}$, respectively [23–24]. In this study, the samples fabricated using Instron, drop hammer, and split Hopkinson bar are denoted as Instron, DH, and SHB, respectively. The flowchart of the test program is illustrated in Fig. 3.

2.2.1. Quasi-static compaction using Instron

In order to investigate the effect of compaction rate, at the beginning, a mixture of powders was prepared under quasi-static compaction through hot press at a strain rate of $8 \times 10^{-3}$ $s^{-1}$ using an Instron testing machine (Fig. 4(a)). Before starting the quasi-static compaction process, it was necessary to determine the optimal compaction pressure to achieve the highest possible densification. As a result, different parameters, including pressure and pressure duration and their effects on compaction, were investigated. To do this, 8 pure Mg samples were compacted at 723 K under pressures of 300 and 600 MPa and for durations of 5, 15, 25, and 35 min. Results showed that the pressure of 600 MPa increased stress level in the die without significantly affecting the quality of samples. The time histories of relative density for the two different compaction pressures are shown in Fig. 4(b). Results revealed that a pressure of 600 MPa, applied for 25 min, yielded the highest relative density. In order to prevent the formation of pores in the samples during cooling, the applied pressure continued until the temperature of the sample reached below 573 K [25].

**Table 1. Specification of the powders used and milling conditions**

| Milling velocity / ($r \cdot min^{-1}$) | Milling time / h | $B_4C$ / vol% | Particle size of Mg / μm | Ball-to-powder mass ratio | Ball size / mm | Stearic acid / wt% | Particle size of $B_4C$ / nm |
|---|---|---|---|---|---|---|---|
| 200 | 1 | 0, 1.5, 3, 5, 10 | 100–150 | 30:1 | 10 | 0.5 | 45 |

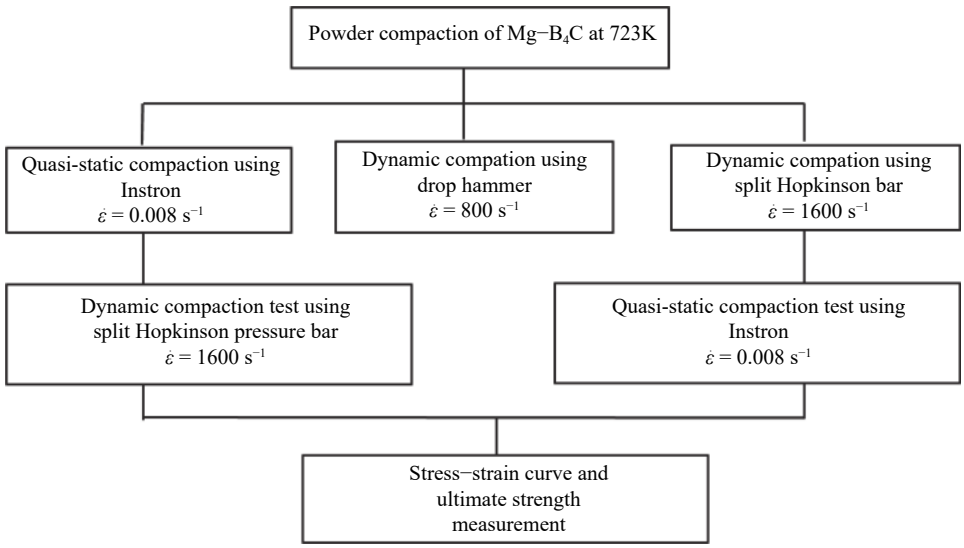


**Fig. 3. Flowchart of the test program.**

2.2.2. Dynamic compaction using a DH

As stated above, a DH was used for dynamic compaction of nanocomposite powders in this work. The impact energy necessary to compact nanocomposite powder was supplied by a mechanical DH with the energy of 2 kJ. This energy was generated by dropping a 60 kg weight from 3.5 m height and was calculated based on the kinetic energy formula $E = MV^2/2$ for the impact velocity of 8 m/s obtained

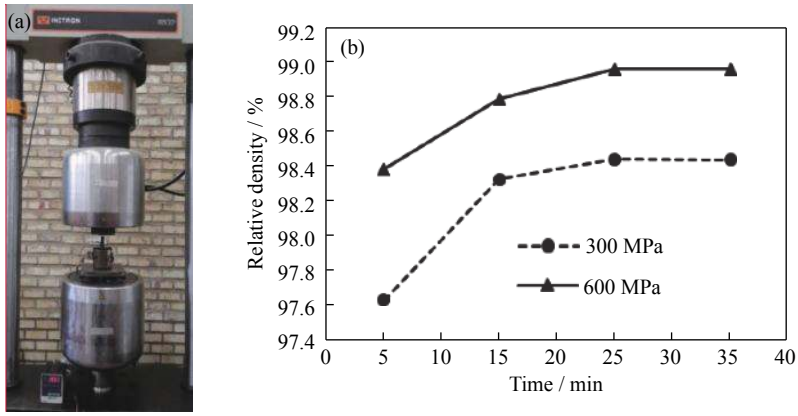


**Fig. 4. Quasi-static hot pressing machine and quasi-static compaction experimental results: (a) Instron testing machine; (b) variations in relative density vs. time for two different compaction pressures.**

from free fall formula $V = \sqrt{2gh}$ (Fig. 5). It was observed that 2 kJ was the best energy for producing the samples. Increasing the energy to approximately 7.3 kJ created cracks and damaged the samples. More details on the mechanism of the DH and powder compaction process have been published [15].

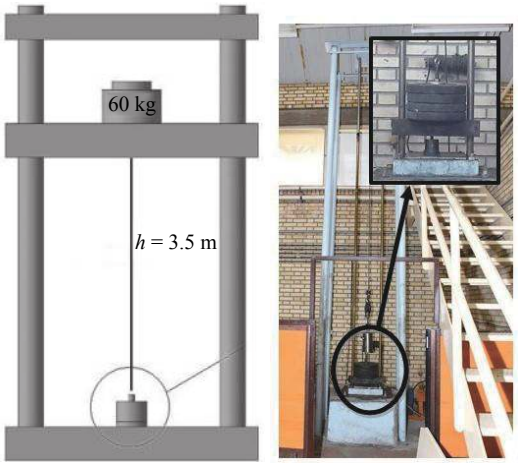


**Fig. 5. Schematic view of the mechanical drop hammer.**

2.2.3. Dynamic compaction using a split Hopkinson bar

A schematic view of the split Hopkinson bar is presented in Fig. 6. Due to the impact energy delivered from the striker to the input bar, the powder was compacted between two bars inside the die. The internal and external diameters of the die were 15 and 60 mm, respectively, and its length was 70 mm. The punch had a diameter of 15 mm and a length of 38 mm, and two disks with a thickness of 5 mm and a diameter of 15 mm were placed above and below the powder. Details of the operation of the split Hopkinson bar and powder compaction mechanism have been reported by Rahmani *et al.* [17]. The impact velocity of the SHB was measured to be 15.5 m/s using a slotted switch-type velocity

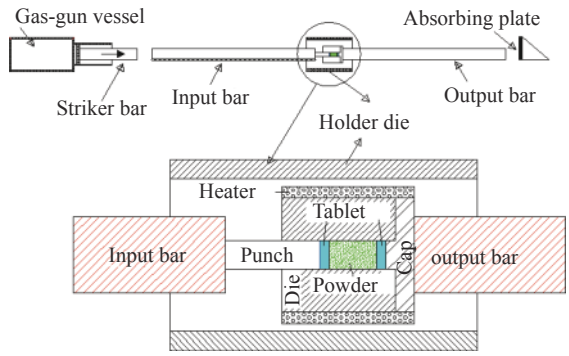


**Fig. 6. Schematic view of the split Hopkinson bar (SHB) arrangement.**

sensor. This velocity created a strain rate of $1.6 \times 10^3$ $s^{-1}$ and kinetic energy of 3.6 kJ, which was sufficient for compacting the powder in the die [17]. This level of kinetic energy for compacting nanocomposite powders was determined by trial and error.

Fig. 7 shows the die and punch used to compact the nanocomposite powders. The internal diameter ($D$) of the die is 15 mm and the height ($H$) of the compacted specimen is 12 mm. Details of the die have been reported by Rahmani *et al.* [17]. All compaction processes were carried out at 723 K using a 1200 W ceramic heating element. This temperature was close to the sintering temperature of magnesi-

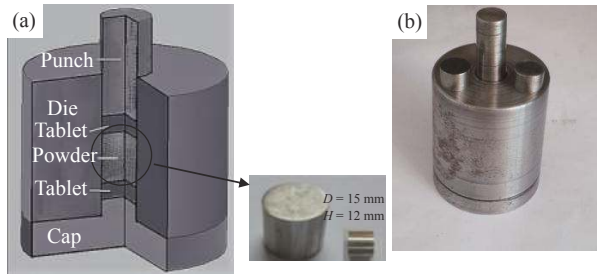


**Fig. 7. Schematic views (a) and final design (b) of the punch and die for compaction of the powder.**

um, which is equal to 75% of the melting point of the metal [26]. 3.5 g of the powder, with density of approximately 55% of theoretical density, was used for compaction. The quality of the nanocomposite mixture was examined using SEM. Further details on the design of the die have been reported by Rahmani *et al.* [17].

## 3. Compression test at different strain rates

### 3.1. Quasi-static compression test

In order to investigate the compressive strength of the compacted samples, uniaxial compression tests were carried out at room temperature and at a strain rate of 0.008 $s^{-1}$ using an Instron testing machine.

### 3.2. Dynamic compression test

A split Hopkinson pressure bar (SHPB) was used to obtain the stress–strain curves of the materials at high strain rates (100–10000 $s^{-1}$) [27]. In this test, the sample was compressed between two long bars made from high strength materials. The SHPB apparatus used in this investigation, the waves propagated in the input and output bars, and the specimen mounted between the two bars is shown in Fig. 8. As can be seen in the figure, three transmitted ($\varepsilon_t(t)$), incident ($\varepsilon_i(t)$), and reflected ($\varepsilon_r(t)$) elastic waves propagated inside the bars as a result of the impact.

The stress, strain, and strain rate of the sample based on the measured transmitted and reflected pulses were calculated using the relations [27]:

$$\begin{cases} \sigma(t) = E\dfrac{A}{A_s}\varepsilon_t(t) \\ \varepsilon(t) = \dfrac{-2C_0}{L}\displaystyle\int_0^t \varepsilon_r(t)\,dt \\ \dot{\varepsilon} = \dfrac{d\varepsilon(t)}{dt} = -\dfrac{C_0[\varepsilon_t(t) - \varepsilon_i(t) + \varepsilon_r(t)]}{L_s} \end{cases} \quad (1)$$

where $A$, $E$, and $C_0$ are the cross-sectional area, elastic modules, and sound speed of the bars, respectively, while $L_s$ and $A_s$ are the length and cross-sectional area of the sample, respectively. The dynamic tests were carried out at striker velocities of 14 to 16 m/s. Based on the sample length (10–12 mm), the strain rate calculated using Eq. (1) was approximately 1600 $s^{-1}$.

## 4. Results and discussion

Ultimate strength was measured from the stress–strain curves of the compacted samples obtained by experiment. The effect of compaction type and strain rate on the ultimate compressive strength (UCS) is investigated in this section.

### 4.1. Morphology of nanocomposite powders

Fig. 9 shows the SEM images of a magnesium particle after mixing and milling with $B_4C$ reinforcement particles at different magnifications. Fig. 9(a) shows the SEM image of the Mg–5vol%$B_4C$ nanocomposite powder. Fig. 9(b) illustrates the distribution of reinforcement particles on the magnesium particles.

### 4.2. Quasi-static compressive tests

Fig. 10 shows the quasi-static stress–strain curves of the samples fabricated using the split Hopkinson bar (SHB), DH, and Instron. As can be seen, the $B_4C$ particles have resulted in significant improvement in the compressive strength of the nanocomposites. Fig. 10(a) indicates an approximate 75% improvement in the UCS of the samples fabricated using the SHB. Improvement was due to the hardness of the nanoparticles and a layer of magnesium oxide (MgO), which has covered the grains and acted as a reinforcement phase [23]. Furthermore, some strengthening mechanisms, such as

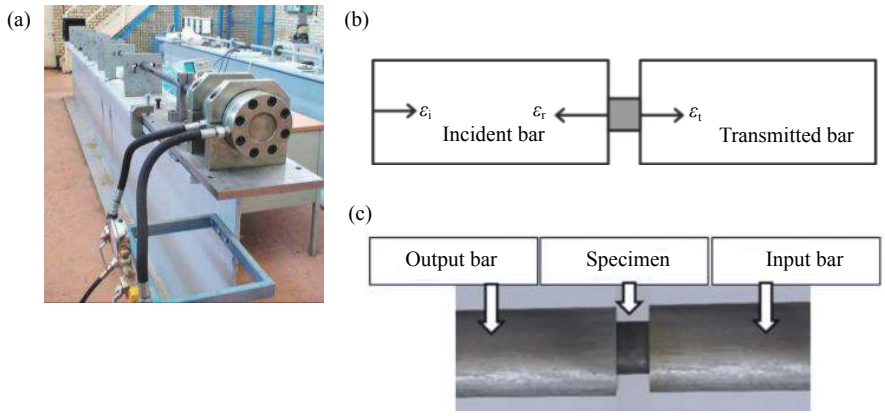


**Fig. 8. SHPB apparatus (a), wave propagation in the input and output bars (b), and the specimen mounted between the two bars (c) used in this investigation.**

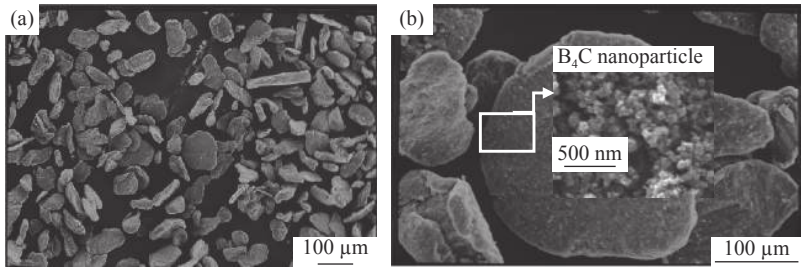


**Fig. 9. SEM images of a magnesium particle after mixing and milling with $B_4C$ reinforcement particles at different magnifications: (a) Mg–5vol%$B_4C$ nanocomposite powder; (b) distribution of the reinforcement particles on the magnesium particles.**

Orowan and thermal mismatch (The large ratio between the thermal expansion coefficients of Mg ($28.4 \times 10^{-6}$ $K^{-1}$) and $B_4C$ ($4.4 \times 10^{-6}$ $K^{-1}$) induces an increased dislocation density) [28–29] have resulted in formation of dislocations that, in turn, have led to increased strength. Based on this mechanism, compressive strength was dependent on particle size and uniformity of the particle distribution. Thermal mismatch was also responsible for the increase in the strength of the nanocomposites with increasing nanoparticle volume fraction [23]. As can be seen in Fig. 10(a), the highest strength was obtained for the SHB samples with 3vol% of reinforcement particles, while a further increase in content of the nanoparticles led to a reduction in strength. The reduction in flow stress for higher contents of nanoparticles could have been due to the higher number of pores in the samples. Fig. 10(b) shows the static stress–strain curves of the samples fabricated using the DH. As can be seen, the UCS increased by 93% for the contents of 3vol% of the nanoparticles. Higher contents gave rise to a decreased UCS. Therefore, the highest compressive strength was achieved for nanocompos-

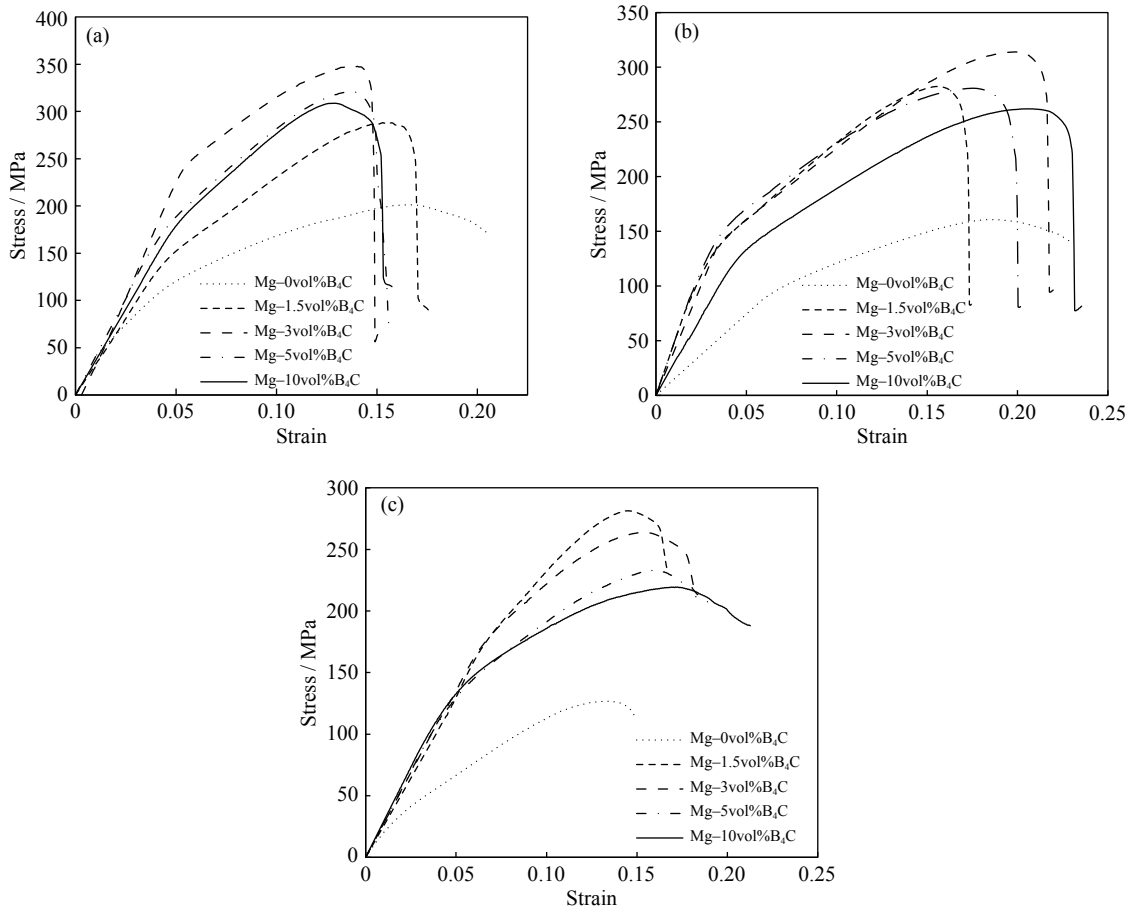


**Fig. 10. Compressive stress–strain curves of pure Mg and Mg–$B_4C$ nanocomposite samples fabricated by (a) SHB, (b) DH, and (c) Instron.**

ites reinforced by a content of 3vol% volume fraction of $B_4C$ compacted at 723 K. Fig. 10(c) shows the stress–strain curves for the samples fabricated using the Instron testing machine. The figure suggests that the UCS increased with increasing $B_4C$ content up to 1.5vol%, after which the compressive strength began to decrease. Therefore, optimal compressive strength could be achieved for nanocomposites reinforced by the content 1.5vol% of $B_4C$ compacted at 723 K. The differences among the optimum $B_4C$ contents obtained from the three different compaction devices could have been due to the different distributions of reinforcement particles and bonds between particles by the three methods. The lower compressive strength of the samples fabricated using Instron compared to the other two devices could have been due to lower melting and weaker bonds between the matrix and reinforcement particles in the samples produced by the Instron testing machine. The weaker bonds were due to insufficient local heating in the quasi-static compaction. Similar results have been reported by Sankaranarayanan *et al.* [30].

Maximum compressive strength and yield stress of the Mg–$B_4C$ nanocomposites fabricated using different methods and obtained from Fig. 10 are illustrated in Fig. 11. As the figures indicate: (1) adding $B_4C$ nanocomposites resulted in an increased UCS and yield strength; (2) there was an optimum for the $B_4C$ content beyond which the strength properties of the Mg–$B_4C$ nanocomposites began to decline; (3) optimum contents were 1.5vol%, 3vol%, and 3vol% for Instron, DH, and SHB, respectively; (4) compressive strength improvements were 124%, 93%, and 75% for Instron, DH, and SHB, respectively.

Data and results were analyzed using a simple rule of mixtures for the composites. In this analysis, the yield stress $\sigma_y$ could be estimated using the following relation [31]:

$$\sigma_y = \sigma_m V_m + \sigma_s V_s \quad (2)$$

where $\sigma_m$ and $\sigma_s$ are the yield stress of the matrix and the second phase, respectively, which are estimated from hardness, and $V_m$ and $V_s$ are the volume fractions of the matrix and second phase, respectively. The highest yield stress was obtained for the Mg–3vol%$B_4C$ nanocomposite fabricated at 723 K using SHB (around $\sigma_y$ = 230 MPa). This stress, which was obtained from the quasi-static stress–strain curves (Fig. 10(a)), agreed well with the estimations from the rule of mixtures and the Tabor equation ($\sigma_y$ = 225 MPa).

Compressive strengths of the Mg–$B_4C$ nanocomposites produced using the three devices are illustrated in Fig. 12. As the figure suggests, the compressive strengths of the samples

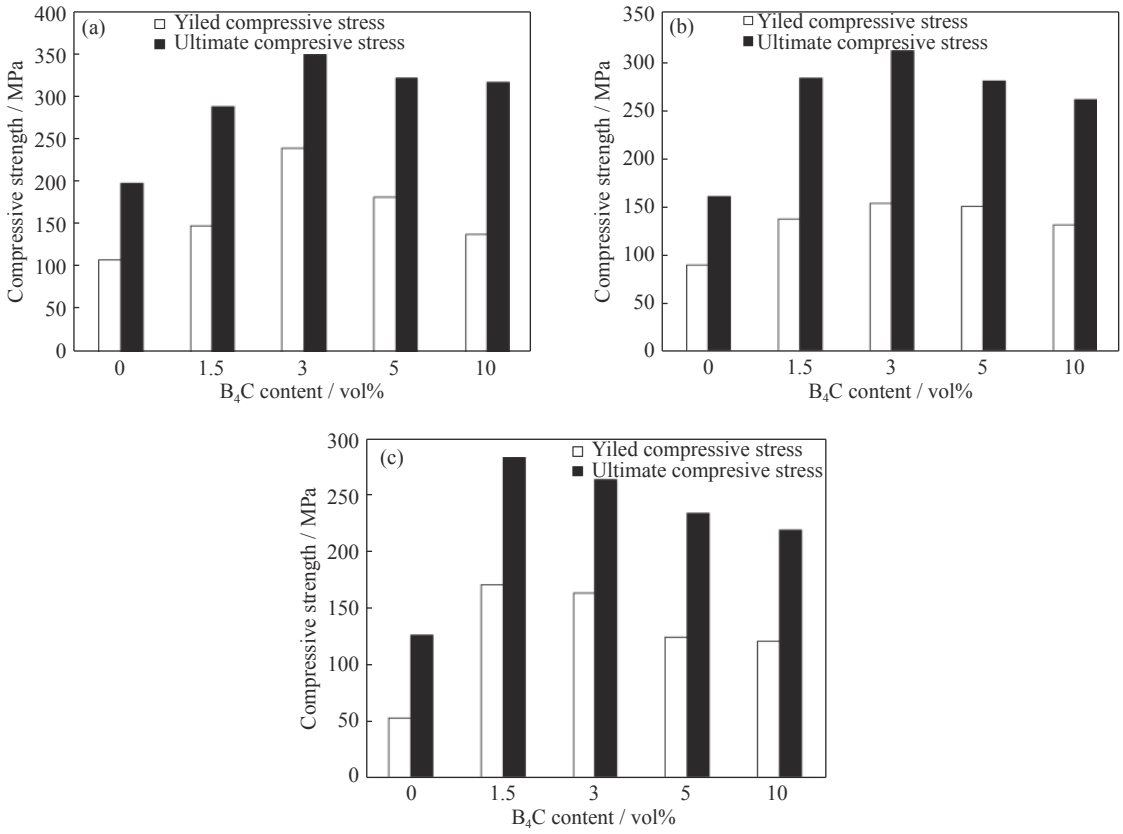


**Fig. 11. Ultimate compressive strength and yield stress of the compacted Mg–$B_4C$ nanocomposite samples fabricated by (a) SHB, (b) DH, and (c) Instron.**

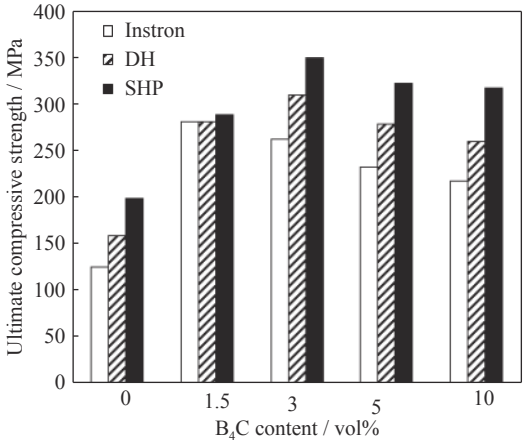


**Fig. 12. Ultimate compressive strength of the compacted Mg–$B_4C$ nanocomposite using different compaction methods.**

fabricated using the SHB were higher than those of the samples fabricated using the DH and Instron. As can be seen in the figure, the highest compressive strength was obtained for the Mg–3vol%$B_4C$ sample produced using the SHB, which was 13% and 33% higher than those obtained using the DH and Instron, respectively.

### 4.3. Dynamic compression tests

Dynamic compression tests were carried out on the samples fabricated by SHB, DH, and Instron using the split Hopkinson pressure bar. Test specimens had a diameter of 15 mm and a length of 12 mm. Each compression test was repeated three times to ensure test repeatability. The dynamic compression stress–strain curves of the nanocomposites fabricated using the three different devices are presented in Fig. 13. Again, and similar to the quasi-static results, the maximum dynamic strength occurred for the 3vol%, 3vol%, and 1.5vol% $B_4C$ for the samples fabricated by SHB, DH, and Instron, respectively. The highest improvement in dynamic strengths, as compared with that of pure Mg, was 61%, 87%, and 90% for SHB, DH, and Instron, respectively.

Variation in UCS versus $B_4C$ nanoparticle content at the strain rates of 0.008 $s^{-1}$ (denoted by LS) and 1600 $s^{-1}$ (denoted by HS) is shown in Fig. 14. As the figure suggests, the compressive strength was influenced by the type of compaction (SHB, DH, or Instron) and the compression test velocity (strain rate). The figure clearly shows that the highest improvement was obtained for the compaction using SHB. The

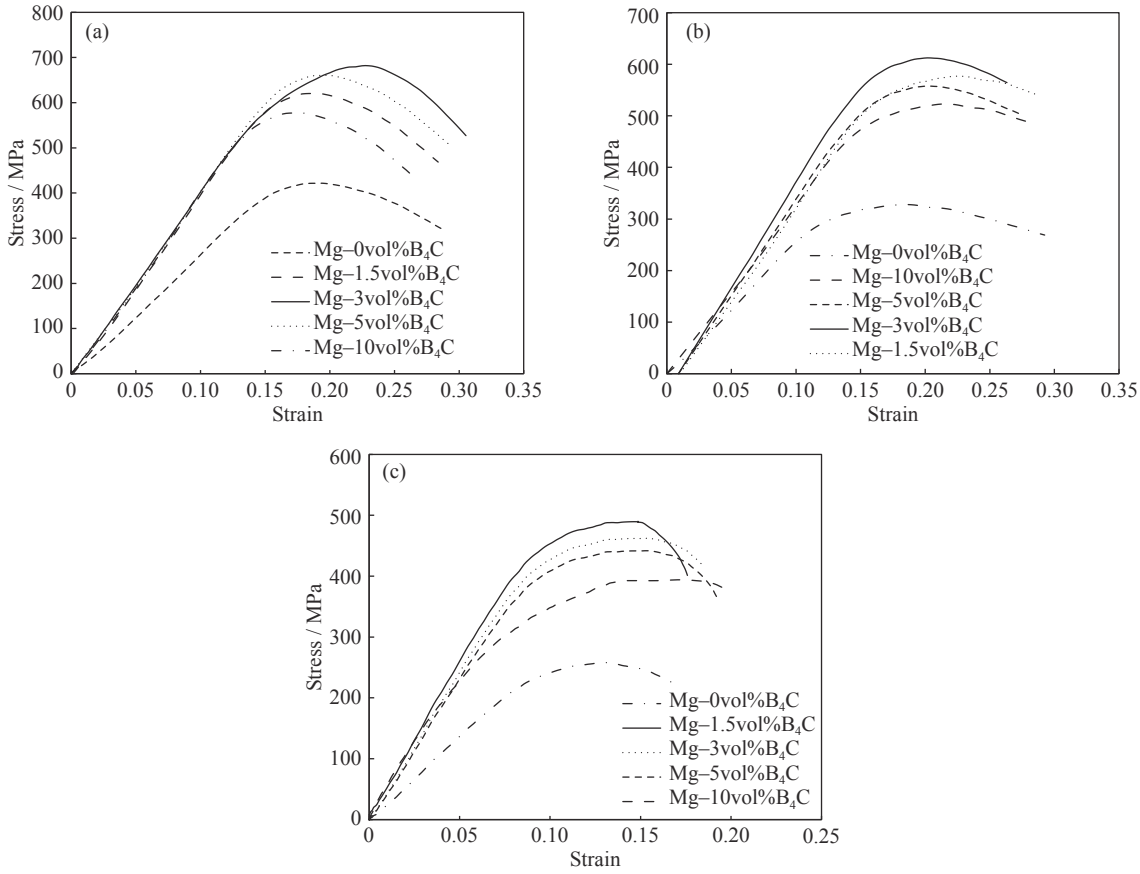


**Fig. 13. Comparison among the compressive stress–strain curves of the samples fabricated by (a) SHB, (b) DH, and (c) Instron at the strain rate of $1.6 \times 10^3$ $s^{-1}$ using SHPB.**

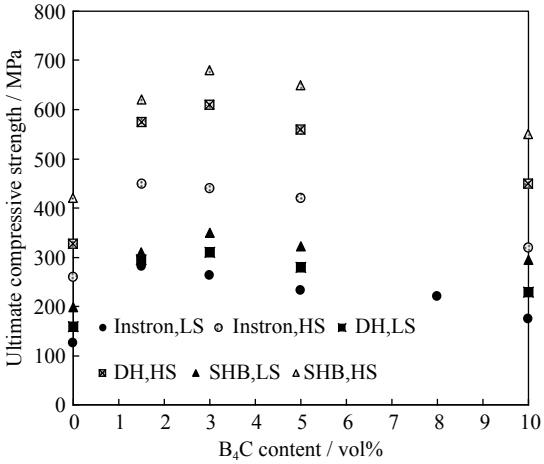


**Fig. 14. Variation in ultimate compressive strength vs. $B_4C$ nanoparticle content at the strain rates of 0.008 and 1600 $s^{-1}$.**

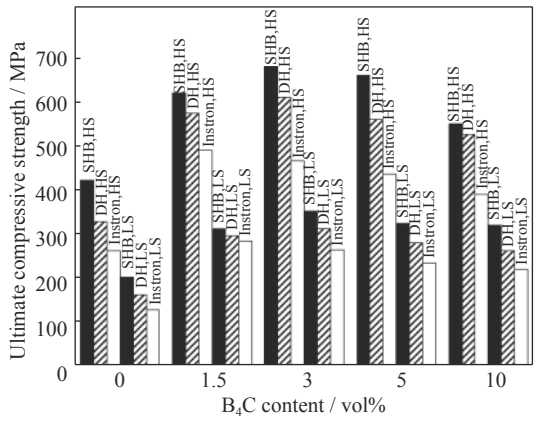


**Fig. 15. Variation in ultimate compressive strength vs. $B_4C$ nanoparticle content at the strain rates of 0.008 and 1600 $s^{-1}$.**

figure also suggests that the highest strength for the SHB compacted samples was obtained at the high strain rate using SHPB.

Variation in UCS versus $B_4C$ nanoparticle content at strain rates of 0.008 and 1600 $s^{-1}$ is shown in Fig. 15. Compressive strength obtained from the quasi-static and split Hopkinson pressure bar compression tests for the samples compacted by Instron, DH, and SHB are given in Table 2. The table clearly shows the influence of the compaction method and compression test speed (strain rate) on the ultimate strength of the samples. Values in the third column are the improvements in UCS for the optimum $B_4C$ content, which was 1.5vol% for the Instron compaction method and 3vol% for the DH and SHB compaction devices with respect to the ultimate strength measured from the quasi-static compression tests and compacted by the Instron testing device (282 MPa). As the table suggests, the improvement in quasi-static strength of the compacted samples was not as significant, and varied from 9.9% for the DH device to 24% for the SHB (the third column of Table 2). However, the effect of the compaction type on the dynamic strength of the samples was remarkable, so that the improvements in dynamic UCS with respect to the Instron strength (282 MPa) were 73%, 116%, and 141% for the specimens compacted by Instron, DH, and SHB, respectively (the fifth column in Table 2).

The sixth column in Table 2 represents the improvement in the ultimate strength obtained from the split Hopkinson pressure bar compression test for each compaction method. For example, the ultimate strength of the specimens compacted by SHB increased from 350 MPa for the quasi-static compression test to 680 MPa for the split Hopkinson pressure bar tests, an improvement of approximately 94%. As can be seen, this improvement was 73%, 96%, and 94%, for Instron, DH, and SHB compaction devices, respectively.

### 4.4. SEM examinations

The presence of hard and rigid particles in a soft matrix reduces the pressability of materials. This reduction in pressability increased with increasing reinforcing phase [32]. Fig. 16 shows the SEM images and porosity of the samples created using the SHB, DH, and Instron at 723 K for different contents of $B_4C$ nanoparticles. As can be seen from the images, the increase in the content of $B_4C$ particles resulted in an increase in the number of pores in the samples. Furthermore, the images clearly show that the porosity of the compacted specimens decreased with increasing strain rate.

Figs. 16(e) and 16(f) clearly show large pores and imperfect compaction in the samples fabricated quasi-statically us-

**Table 2. Compressive strengths obtained for various compaction methods and compression strain rates for the optimum $B_4C$ content**

| Compaction method | Quasi-static strength (0.008 $s^{-1}$) / MPa | UCS improvement with respect to quasi-static | Split Hopkinson pressure bar strength (1600 $s^{-1}$) / MPa | Improvement in dynamic UCS with respect to the Instron strength | Improvement in dynamic UCS with respect to the quasi-static UCS |
|---|---|---|---|---|---|
| Instron, LS | 282 | — | 490 | 73% | 73% |
| DH, LS | 310 | 9.9% | 610 | 116% | 96% |
| SHB, HS | 350 | 24% | 680 | 141% | 94% |

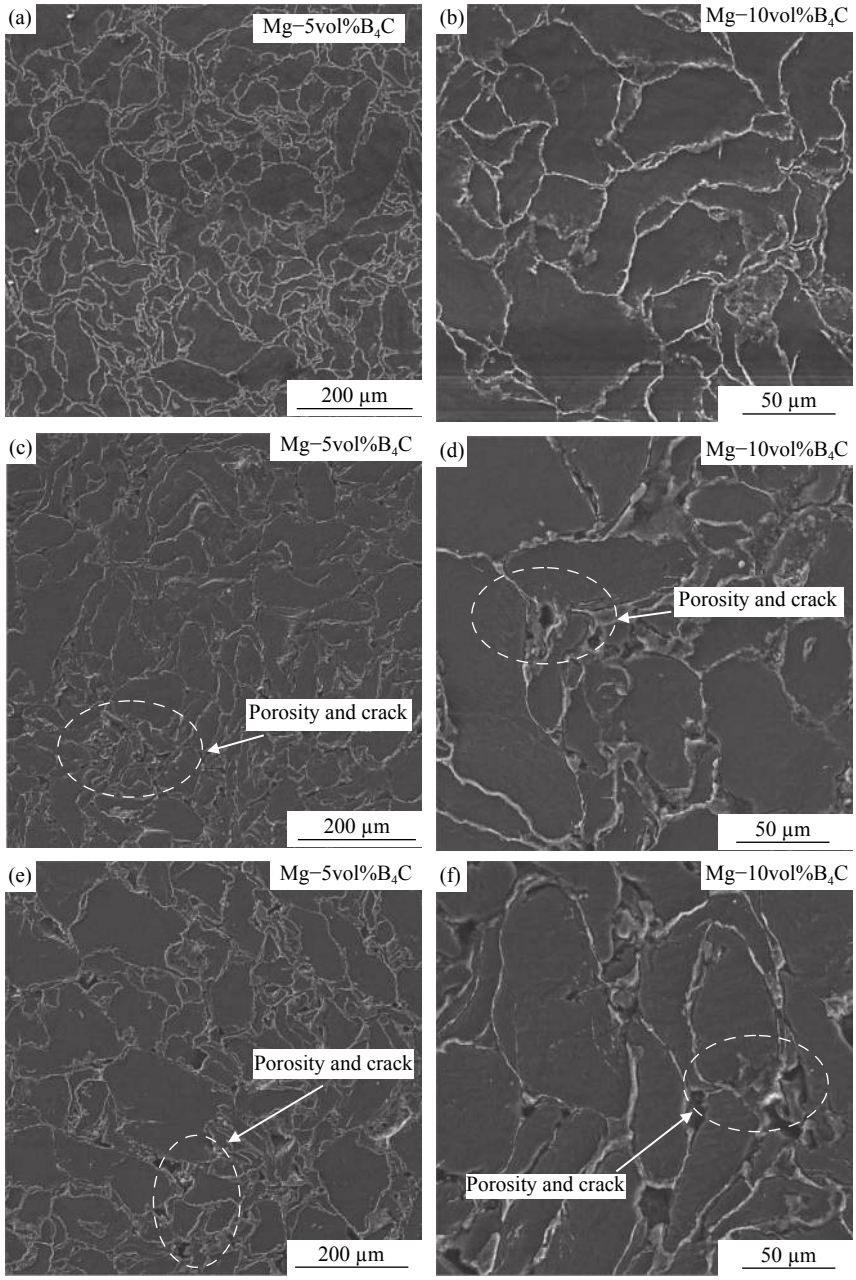


**Fig. 16. SEM micrographs of the specimens compacted using (a, b) SHB, (c, d) DH, and (e, f) Instron.**

ing Instron. Figs. 16(e) and 16(f) also demonstrate that the size of the pores and their distances decreased by changing the compaction device from Instron to SHB. Furthermore, many of the pores and grain boundaries disappeared in the samples compacted by the SHB compared to the samples compacted by Instron or the DH. This implied that compaction using the SHB gave rise to a perfect sintering largely due to the adiabatic temperature rise from the friction between the particles. This was induced by the high impact energy transferred to the particles. This energy caused high velocity relative movements of the particles with respect to each other and high rates of deformation at the particles surfaces. The energy, in fact, produced large strain rates and, therefore, the process was considered as adiabatic, i.e., the energy converted to heat did not have enough time to dissipate, generating internal heat brings with the local temperature rise in the powder, and softening the particle surfaces, a phenomenon known as thermal softening. On the other hand, the friction due to the movement of the particles accelerates the localized temperature rise that, in turn, caused plastic deformation and softening of the surface layer of the particles. This phenomenon improved the bonding between the particles and brought about a further increase in consolidation [12].

There could have been two reasons for the perfect compaction obtained using the SHB. The first was that two areas of the specimen underwent high local pressure: the surface of the powder particles, which was affected by back and forth waves, and the area affected by the shock transfer from the high impedance striker to the punch, which was aligned with the low impedance powder [33]. The high stress waves caused cracks, cavities, and pores, and produced low-porous and high-densified compaction. Of course, it was evident from the elementary impact mechanics that some incident and transmitted waves reflected in tensile mode, which, in turn, created new pores and cracks [34].

The second reason for the relatively high compaction was friction and adiabatic heating. Meyers *et al.* [35] investigated different phenomena resulting from shockwave compaction including aggregate and inter-particle plastic deformation, friction, and local melting between particles. They stated that all these parameters act together at the same time. For instance, kinetic energy generated due to fast movement and deformation of the powders can lead to adiabatic heating and local melting and sintering, while the friction among powder particles can increase mechanical bonding among powder particles. Furthermore, the adiabatic heat created during impact compaction can increase the local temperature of the powder's surface, resulting in softening of the surface and facilitating mechanical bonding [36]. Meyers [37] also reported that dynamic compaction has a higher dislocation density compared to quasi-static compaction methods.

## 5. Conclusions

Mg−$B_4C$ nanocomposites were produced through hot compaction technique using 0, 1.5vol%, 3vol%, 5vol%, and 10vol% $B_4C$ nanoparticles at a temperature of 723 K using SHB, DH, and Instron testing. Stress–strain curves of the compacted samples were captured under quasi-static and dynamic loadings using Instron and a split Hopkinson pressure bar, respectively. The results revealed that:

(1) There was an optimum for the $B_4C$ content to achieve the maximum improvement in ultimate compressive strength for the nanocomposite samples. Optimum contents for the samples produced by Instron, DH, and SHB were 1.5vol%, 3vol%, and 3vol%, respectively. Compressive strength improvements (with respect to the strength of pure Mg) obtained from the quasi-static stress–strain curves for the samples produced by Instron, DH, and SHB were 124%, 93%, and 75%, respectively.

(2) Effect of compaction type on the ultimate strength obtained from the quasi-static stress–strain curves of the samples was not as significant, and only varied from 9.9% for DH to 24% for SHB, relative to that for quasi-statically compacted specimens reinforced by the optimum $B_4C$ content.

(3) Effect of compaction type on the dynamic strengths of the samples was remarkable so that the strengths were improved (with respect to strength of the quasi-statically compacted specimens reinforced by the optimum $B_4C$ content) by 73%, 116%, and 141% for the specimens compacted by Instron, DH, and SHB, respectively.

(4) Improvement in strength is believed to have been due to strengthening mechanisms including the Orowan mechanism and the increase in dislocation density due to the thermal mismatch phenomenon, friction, adiabatic heating, and shock waves created by the SHB.

## References

[1] Q.B. Nguyen and M. Gupta, Improving compressive strength and oxidation resistance of AZ31B magnesium alloy by addition of nano-$Al_2O_3$ particulates and Ca, *J. Compos. Mater.*, 44(2010), No. 7, p. 883.

[2] M. Gupta, M.O. Lai, and D. Saravanaranganathan, Synthesis, microstructure and properties characterization of disintegrated melt deposited Mg/SiC composites, *J. Mater. Sci.*, 35(2000), No. 9, p. 2155.

[3] A. Ahmed, A.J. Neely, K. Shankar, P. Nolan, S. Moricca, and T. Eddowes, Synthesis, tensile testing, and microstructural characterization of nanometric SiC particulate-reinforced Al 7075 matrix composites, *Metall. Mater. Trans. A*, 41(2010), No. 6, p. 1582.

[4] R. Harichandran and N. Selvakumar, Effect of nano/micro $B_4C$ particles on the mechanical properties of aluminium metal matrix composites fabricated by ultrasonic cavitation-assisted solidification process, *Arch. Civ. Mech. Eng.*, 16(2016), No. 1, p. 147.

[5] A. Ganguly, S. Sharma, P. Papakonstantinou, and J. Hamilton, Probing the thermal deoxygenation of graphene oxide using high-resolution *in situ* X-ray-based spectroscopies, *J. Phys. Chem. C*, 115(2011), No. 34, p. 17009.

[6] I. Khelifa, A. Belmokhtar, R. Berenguer, A. Benyoucef, and E. Morallon, New poly (o-phenylenediamine)/modified-clay nanocomposites: A study on spectral, thermal, morphological and electrochemical characteristics, *J. Mol. Struct.*, 1178(2019), p. 327.

[7] S. Daikh, F.Z. Zeggai, A. Bellil, and A. Benyoucef, Chemical polymerization, characterization and electrochemical studies of PANI/ZnO doped with hydrochloric acid and/or zinc chloride: Differences between the synthesized nanocomposites, *J. Phys. Chem. Solids*, 121(2018), p. 78.

[8] S. Benyakhou, A. Belmokhtar, A. Zehhaf, and A. Benyoucef, Development of novel hybrid materials based on poly (2-aminophenyl disulfide)/silica gel: preparation, characterization and electrochemical studies, *J. Mol.*

*Struct.*, 1150(2017), p. 580.

[9] K. Rahmani and G.H. Majzoobi, An investigation on SiC volume fraction and temperature on static and dynamic behavior of Mg−SiC nanocomposite fabricated by powder metallurgy, *Modares Mech. Eng.*, 18(2018), No. 3, p. 361.

[10] A. Abdollahi, A. Alizadeh, and H.R. Baharvandi, Dry sliding tribological behavior and mechanical properties of Al2024–5wt%$B_4C$ nanocomposite produced by mechanical milling and hot extrusion, *Mater. Des.*, 55(2014), p. 471.

[11] R.M. Mohanty, K. Balasubramanian, and S.K. Seshadri, Boron carbide-reinforced alumnium 1100 matrix composites: fabrication and properties, *Mater. Sci. Eng. A*, 498(2008), No. 1-2, p. 42.

[12] J.Z. Wang, X.H. Qu, H.Q. Yin, M.J. Yi, and X.J. Yuan, High velocity compaction of ferrous powder, *Powder Technol.*, 192(2009), No. 1, p. 131.

[13] W.H. Gourdin, Dynamic consolidation of metal powders, *Prog. Mater Sci.*, 30(1986), No. 1, p. 39.

[14] A.N. Faruqui, P. Manikandan, T. Sato, Y. Mitsuno, and K. Hokamoto, Mechanical milling and synthesis of Mg−SiC composites using underwater shock consolidation, *Met. Mater. Int.*, 18(2012), No. 1, p. 157.

[15] G.H. Majzoobi, K. Rahmani, and A. Atrian, Temperature effect on mechanical and tribological characterization of Mg−SiC nanocomposite fabricated by high rate compaction, *Mater. Res. Express*, 5(2018), No. 1, art. No. 015046 .

[16] G.H. Majzoobi, K. Rahmani, and A. Atrian, An experimental investigation into wear resistance of Mg−SiC nanocomposite produced at high rate of compaction, *J. Stress Anal.*, 3(2018), No. 1, p. 35.

[17] K. Rahmani, G.H. Majzoobi, and A. Atrian, A novel approach for dynamic compaction of Mg–SiC nanocomposite powder using a modified Split Hopkinson Pressure Bar, *Powder Metall.*, 61(2018), No. 2, p. 164.

[18] Q.C. Jiang, H.Y. Wang, B.X. Ma, Y. Wang, and F. Zhao, Fabrication of $B_4C$ particulate reinforced magnesium matrix composite by powder metallurgy, *J. Alloys Compd.*, 386(2005), No. 1-2, p. 177.

[19] M. Aydin, R. Koç, and A. Akkoyunlu, Fabrication and characterisation of Mg-nano $B_4C$ and B composites by powder metallurgy method, *Adv. Mater. Process. Technol.*, 1(2015), No. 1-2, p. 181.

[20] I. Aatthisugan, A.R. Rose, and D.S. Jebadurai, Mechanical and wear behaviour of AZ91D magnesium matrix hybrid composite reinforced with boron carbide and graphite, *J. Magnesium Alloys*, 5(2017), No. 1, p. 20.

[21] V. Kevorkijan and S.D. Škapin, Mg/$B_4C$ composites with a high volume fraction of fine ceramic reinforcement, *Mater. Manuf. Processes*, 24(2009), No. 12, p. 1337.

[22] Y.T. Yao, L. Jiang, G.F. Fu, and L.Q. Chen, Wear behavior and mechanism of $B_4C$ reinforced Mg-matrix composites fabricated by metal-assisted pressureless infiltration technique, *Trans. Nonferrous Metal. Soc. China*, 25(2015), No. 8, p. 2543.

[23] K. Rahmani, G.H. Majzoobi, and A. Atrian, Simultaneous effects of strain rate and temperature on mechanical response of fabricated Mg–SiC nanocomposite, *J. Compos. Mater.*, 2019, art. No. 0021998319864629.

[24] G.H. Majzoobi, A. Atrian, and M.K. Pipelzadeh, Effect of densification rate on consolidation and properties of Al7075–$B_4C$ composite powder, *Powder Metall.*, 58(2015), No. 4, p. 281.

[25] M. Tavoosi, F. Karimzadeh, M.H. Enayati, and A. Heidarpour, Bulk Al–Zn/$Al_2O_3$ nanocomposite prepared by reactive milling and hot pressing methods, *J. Alloys Compd.*, 475(2009), No. 1-2, p. 198.

[26] A. Atrian, G.H. Majzoobi, M.H. Enayati, and H. Bakhtiari, Mechanical and microstructural characterization of Al7075/SiC nanocomposites fabricated by dynamic compaction, *Int. J. Miner. Metall. Mater.*, 21(2014), No. 3, p. 295.

[27] G.H. Majzoobi, F. Freshteh-Saniee, S.F.Z. Khosroshahi, and H.B. Mohammadloo, Determination of materials parameters under dynamic loading. Part I: Experiments and simulations, *Comput. Mater. Sci*, 49(2010), No. 2, p. 192.

[28] S.F. Hassan and M. Gupta, Effect of submicron size $Al_2O_3$ particulates on microstructural and tensile properties of elemental Mg, *J. Alloys Compd.*, 457(2008), No. 1-2, p. 244.

[29] Z.Q. Mo, Y.Z. Liu, J.J. Geng, and T. Wang, The effects of temperatures on microstructure evolution and mechanical properties of $B_4C$–AA2024 composite strips prepared by semi-solid powder rolling, *Mater. Sci. Eng. A*, 652(2016), p. 305.

[30] S. Sankaranarayanan, M.K. Habibi, S. Jayalakshmi, K.J. Ai, A. Almajid, and M. Gupta, Nano-AlN particle reinforced Mg composites: Microstructural and mechanical properties, *Mater. Sci. Technol.*, 31(2015), No. 9, p. 1122.

[31] C.T. Wei, E. Vitali, F. Jiang, S.W. Du, D.J. Benson, K.S. Vecchio, N.N. Thadhani, and M.A. Meyers, Quasi-static and dynamic response of explosively consolidated metal–aluminum powder mixtures, *Acta Mater.*, 60(2012), No. 3, p. 1418.

[32] W.B. Eisen, B.L. Ferguson, R.M. German, R. Iacocca, P.W. Lee, D. Madan, K. Moyer, H. Sanderow, and Y. Trudel, *Powder Metal Technologies and Applications*, ASM International, USA, 1998.

[33] D. Yim, W. Kim, S. Praveen, M.J. Jang, J.W. Bae, J. Moon, E. Kim, S.T. Hong, and H.S. Kim, Shock wave compaction and sintering of mechanically alloyed CoCrFeMnNi high-entropy alloy powders, *Mater. Sci. Eng. A*, 708(2017), p. 291.

[34] R.L. Williamson, Parametric studies of dynamic powder consolidation using a particle-level numerical model, *J. Appl. Phys.*, 68(1990), No. 3, p. 1287.

[35] M.A. Meyers, D.J. Benson, and E.A. Olevsky, Shock consolidation: microstructurally-based analysis and computational modeling, *Acta Mater.*, 47(1999), No. 7, p. 2089.

[36] K.I. Kondo, S. Soga, A. Sawaoka, and M. Araki, Shock compaction of silicon carbide powder, *J. Mater. Sci.*, 20(1985), No. 3, p. 1033.

[37] M.A. Meyers, A mechanism for dislocation generation in shock-wave deformation, *Scripta Metall.*, 12(1978), No. 1, p. 21.